

Mitochondria, unique organelles that are compartmentalized by outer (MOM) and inner (MIM) membrane bilayers, are the cellular powerhouses of eukaryotes. In addition to their primary function as energy producers via the generation of ATP by aerobic respiration¹, mitochondria participate in a wide variety of crucial cellular processes, such as apoptosis^{2,3}, calcium homeostasis^{4,5}, cell signalling⁶ and ageing⁷.

Recent research has revealed that mitochondria act as a central hub for cellular innate immunity in vertebrates, particularly mammals^{8–10}. The link between mitochondria and innate immunity was initially discovered based on the activation of the retinoic acid-inducible gene I (RIG-I)-like receptors (RLRs) signal transduction pathway that leads to the production of type I interferons (IFNs) and proinflammatory cytokines as the first line of defence against RNA viruses. In this signalling pathway, cytoplasmic virus-derived RNA that gains entry into the host cell is recognized by RLRs, and the protein-nucleotide complex translocates to the mitochondrial antiviral signalling protein (MAVS)¹¹, followed by the recruitment of various downstream signalling effectors on the MOM to form a supramolecular assembly essential for immune responses^{8–10}. In addition to their involvement with host cell defence via the RLRs pathway, mitochondria are also involved in other types of inflammation, such as the activation of the NOD-like receptor (NLR) family pyrin domain-containing 3 (NLRP3) inflammasomes. NLRP3 inflammasomes are activated by sensing mitochondrial reactive oxygen species^{12,13} that are generated through mitochondrial respiration, or by cytosolic mitochondrial DNA that are released from damaged organelles¹⁴, which results in the secretion of inflammasome-dependent cytokines, such as interleukin-1 β (IL-1 β) and IL-18. Although these mitochondrial-mediated immune responses are tissue/cell type-specific and primed by different stimuli, the convergence of multiprotein complexes on the MOM surface is a key process of each signalling event, thereby promoting the development of immune responses^{8–10,15}.

Our previous studies demonstrated that the mitochondrial membrane potential ($\Delta\psi_m$), a fundamental mitochondrial phenomenon, is essential to activate both the RLRs pathway and NLRP3 inflammasomes against viral infection^{16,17}. An interesting aspect of these findings is that $\Delta\psi_m$ across the MIM and the supramolecular signalling assembly on the MOM platform that is topologically flanked by the biological membrane is coupled and activates the immune response in concert. However, the physiological relevance of $\Delta\psi_m$ in innate immunity has not been elucidated given that previous studies were mostly performed under chemical treatment using the protonophore, carbonyl cyanide *m*-chlorophenylhydrazone (CCCP)^{16,17}.

PB1-F2 (ref. 18), an influenza A viral protein that is encoded in most influenza A viral strains in the +1 alternate open-reading frame of the RNA polymerase subunit (PB1 gene segment), can be expressed as several different polypeptide lengths with a full size of predominantly 87 or 90 amino acids¹⁹ (Supplementary Fig. 1a). An intriguing genomic feature of PB1-F2 is that the highly pathogenic strains (for example, H5N1 subtype) express a longer polypeptide that contains most of the 90 amino acids of PB1-F2, whereas the low pathogenic subtypes (for example, H1N1, with the exception of the 1918 pandemic strain) tend to express a shorter version containing 57 amino acids known as C-terminal truncated form (Supplementary Fig. 1b). Although the PB1-F2 derived from the A/Puerto-Rico/8 (denoted A/PR8 (H1N1)) strain, which has 87 amino acids (longer polypeptide), is known to localize in mitochondria^{18,20–22} and induce apoptosis^{18,22}, the mechanisms by which it translocates into mitochondria and affects the immune response remain unclear.

In the present study, we investigated the mechanistic and functional roles of PB1-F2 in mitochondrial-mediated innate immunity. We observed that PB1-F2 translocation into mitochondria leads to $\Delta\psi_m$ attenuation that strongly correlated with impaired cellular innate immunity.

Results

Distinct subcellular localization of PB1-F2 variants. We first confirmed the specificity of PB1-F2 in associating with mitochondria rather than other organelles, such as the endoplasmic reticulum (ER) and/or peroxisomes. Using a biochemical approach, we fractionated the cell extract from A/PR8-infected cells. The translated PB1-F2 polypeptide in infected HEK293 cells was predominantly observed in the heavy membrane fraction, which contains mitochondrial proteins, and not in the light microsomal membrane or cytosolic fractions (Fig. 1a). Because the infected cells also express other viral proteins that might bypass PB1-F2 targeting to the heavy membrane fraction, we next confirmed whether the protein alone was sufficient to be fractionated into the heavy membrane. As expected, a similar trend was observed in cellular extracts from transiently transfected cells (Supplementary Fig. 2; top panel, PR8). To verify that the observed results were not due to unique characteristics of the viral strain used, we repeated the same experiment using other PB1-F2 variants originating from a different strain (A/California(CA)/04/09 (H1N1) mutants)²³ and demonstrated that those variants were also exclusively present in the heavy membrane fraction (Supplementary Fig. 2; 88W and 58W). By contrast, a C-terminal truncated version of PB1-F2 encoding 57 amino acids (denoted 12S), a major population of the low pathogenic subtype, was predominantly observed in the cytosolic fraction. Immunofluorescence microscopy supported these biochemical observations. Consistent with previous reports^{20,21}, the full-length proteins (PR8, 88W and 58W) clearly localized to mitochondria (but not to other organelles, including the ER and peroxisomes; Fig. 1b), and the N66S polymorphism²⁴ in PB1-F2 did not affect its subcellular localization (Supplementary Fig. 3). However, the 12S variant was diffusely localized to the cytoplasm (Fig. 1b). The observed affinity of the full-length PB1-F2 variants for mitochondria was further corroborated using an *in vitro* import assay (Fig. 1c).

Full-length PB1-F2 localizes to the inner membrane space. We then analyzed the sub-mitochondrial localization of the PB1-F2 variants. When mitochondria isolated from PB1-F2-expressing cells were treated with a high-salt buffer (1 M KCl), none of the variants were extracted from the pellet (Fig. 2a), suggesting that PB1-F2 did not associate with the MOM via electrostatic interactions. Hypotonic swelling of mitochondria also failed to release PB1-F2 into the supernatant (Fig. 2b), demonstrating that the protein was either in the matrix or integrated and/or tightly associated with the MIM. Sucrose density gradient centrifugation demonstrated that PB1-F2 co-fractionates with CoxIV, an intrinsic MIM protein (Fig. 2c). However, treatment of the mitochondrial pellet with an alkaline solution (pH 11.5) allowed us to extract PB1-F2 (partially) and unanchored mitochondrial proteins (Cyt c, AIF and Hsp60) from the soluble fraction (Fig. 2a; far right lanes). The behaviour of these proteins was distinct from that of the integrated MOM or MIM proteins (Mfn1, Mfn2, Tom20 and CoxIV).

We confirmed that PB1-F2 was resistant to proteinase K digestion in the absence of digitonin, whereas it was completely digested in the presence of a low digitonin concentration that specifically permeabilizes the MOM, excluding the possibility that PB1-F2 was localized to the matrix side (Fig. 2d). The viral

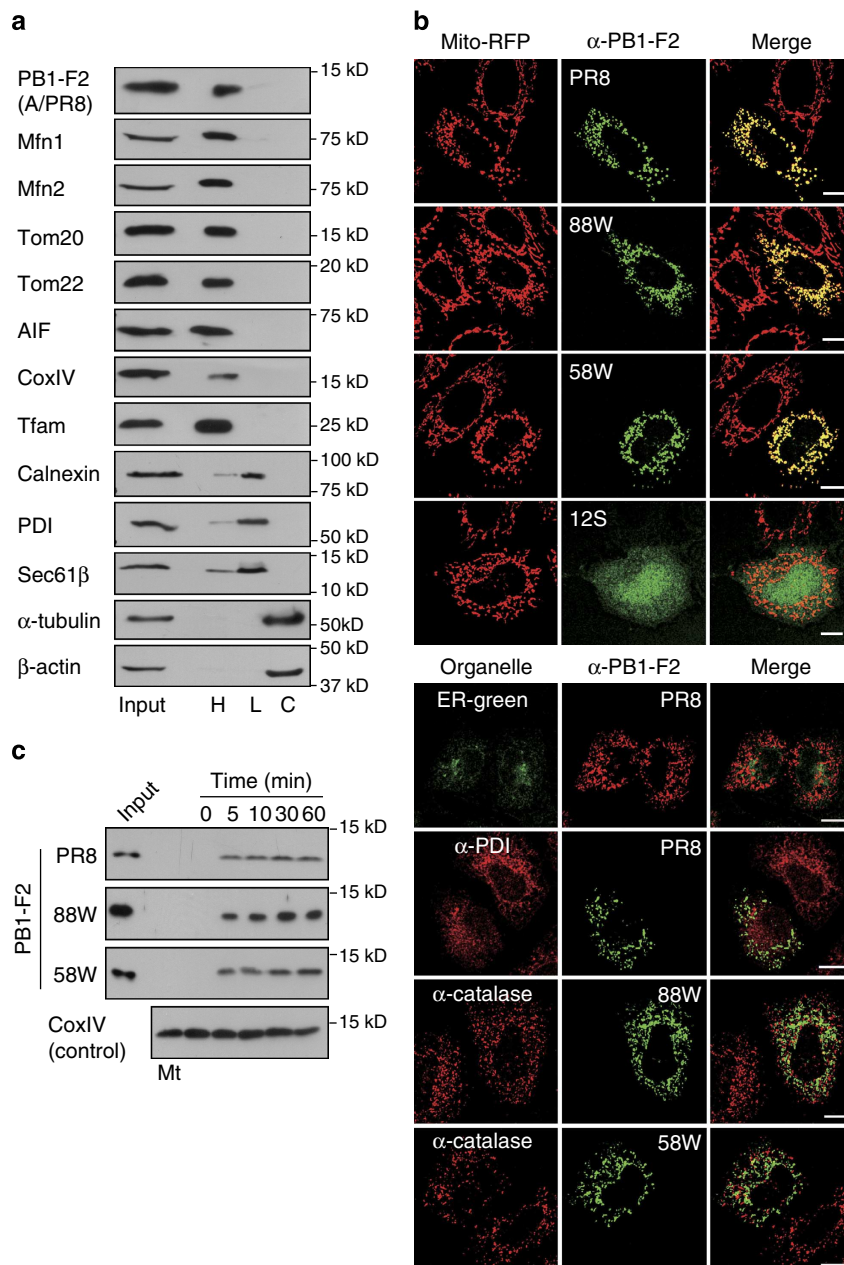


Figure 1 | Full-length PB1-F2 variants associate with mitochondria. (a) Cellular fractions from A/PR8 (16 HA U ml^{-1})-infected HEK293 cells were collected by differential centrifugation and analyzed by Western blotting using the indicated organelle markers. C, cytosolic fraction; H, heavy membrane fraction; L, light microsomal membrane fraction. (b) Subcellular localization of PB1-F2 variants. The indicated constructs (PR8, 88W, 58W and 12S) were expressed in HeLa cells, and immunofluorescence with PB1-F2 specific antibodies was used to detect expression (middle panels). Mitochondria in the same cells were identified by stable expression of mitochondrially targeted red fluorescent protein (Mito-RFP, left panels). The bottom four rows depict other organelle markers for the endoplasmic reticulum (ER-green and anti-PDI) and peroxisomes (anti-catalase). Scale bar, $10 \mu\text{m}$. (c) Each full-length PB1-F2 variant was synthesized *in vitro* and incubated with isolated mitochondria (Mt) from HEK293 cells for the indicated times at 25°C . The reactants were then treated with proteinase K and analyzed by Western blotting. Bottom panel, CoxIV was used as a loading control.

protein topology was further confirmed using semi-permeabilized cells²⁵ to monitor the accessibility of PB1-F2 antibodies. PB1-F2 was visible when the MOM was specifically permeabilized by a low digitonin concentration (compare Supplementary Fig. 4a,b), which was consistent with the proteolysis results. We then analyzed the structural characteristics of the conformation of mitochondrially targeted PB1-F2 using a bioluminescence resonance energy transfer (BRET)-based assay²⁶ in live cells. The interaction between Venus- and NanoLuc luciferase

(NLuc)-tagged PB1-F2 but not other Venus-tagged proteins was successfully monitored (Supplementary Fig. 5). This homotypic interaction combined with a complementation assay (biomolecular fluorescence complementation)²⁶ revealed that the PB1-F2 complex is composed of more than three molecules (Fig. 2e). Taken together, these biochemical lines of evidence indicate that PB1-F2 constitutively localizes to the mitochondrial inner membrane space (IMS), is tightly associated with the MIM, and assembles into a highly ordered oligomer.

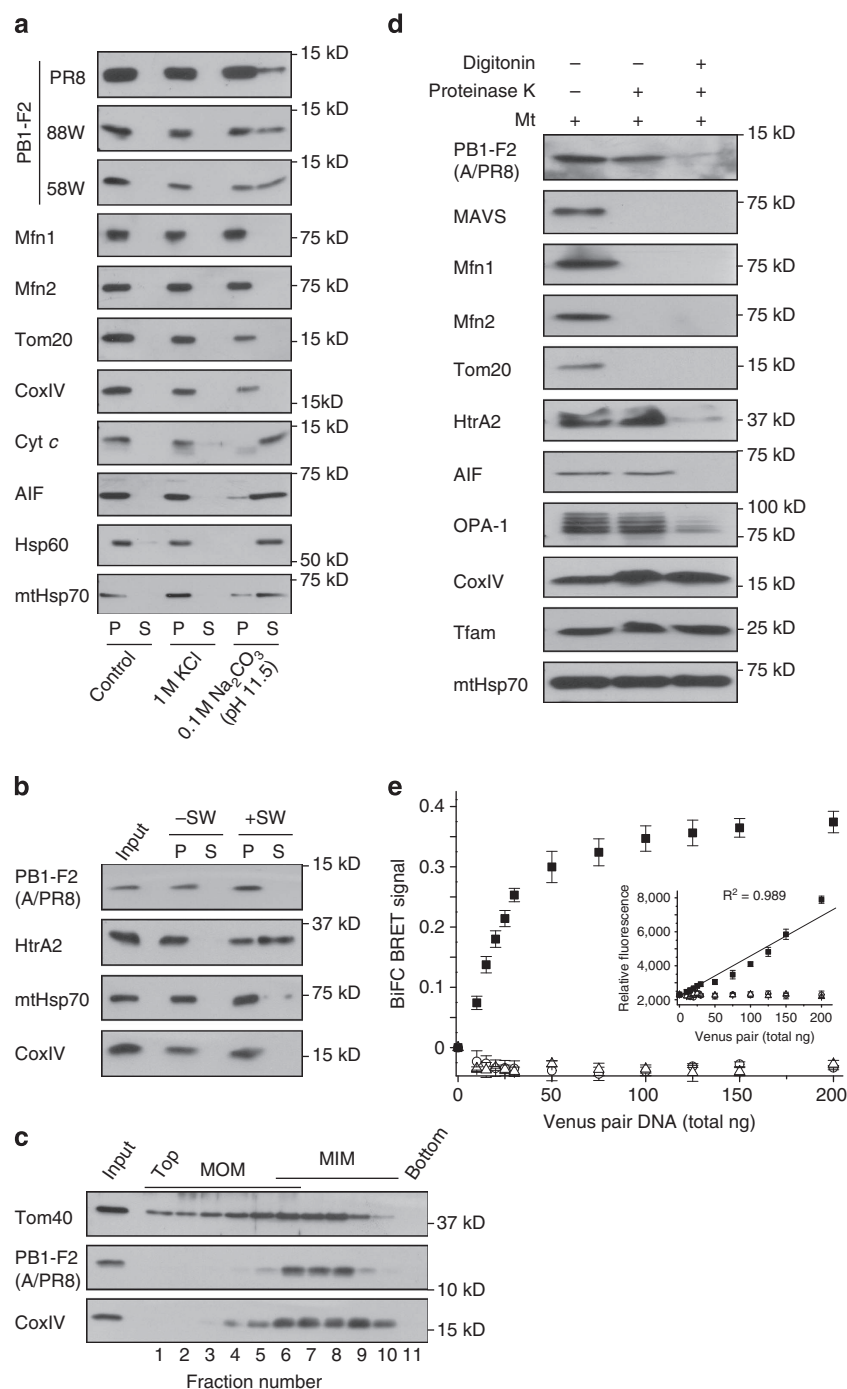


Figure 2 | PB1-F2 translocates into the mitochondrial inner membrane space. (a) Isolated mitochondria from PB1-F2-expressing HEK293 cells were treated with either 1 M KCl or 0.1 M Na₂CO₃ (pH 11.5) for 30 min on ice. After centrifugation, the supernatant (S) and pellets (P) were analyzed by immunoblotting with antibodies against PB1-F2 or several mitochondrial proteins as indicated. (b) Mitochondria isolated from A/PR8 (16 HA U ml⁻¹)-infected HEK293 cells were diluted into either regular (-SW) or hypotonic swelling (+SW) buffer and maintained on ice for 30 min. After centrifugation, the supernatant (S) and pellets (P) were analyzed by Western blotting using the indicated sub-mitochondrial markers. HtrA2 was used as a positive control for an unanchored IMS protein. CoxIV and mtHsp70 are MIM and matrix proteins, respectively. (c) Sub-mitochondrial fractionation of PB1-F2 (A/PR8) by sucrose density gradient centrifugation. After centrifugation, fractions (numbered) were analyzed by Western blotting with antibody against PB1-F2 or against indicated sub-mitochondrial markers. (d) The mitochondrial fraction isolated from A/PR8 (16 HA U ml⁻¹)-infected HEK293 cells was treated with proteinase K (100 µg ml⁻¹) in the absence or presence of 500 µg ml⁻¹ digitonin (pre-permeabilized condition) for 15 min on ice. The reactants were developed by immunoblotting with antibodies against PB1-F2 or against several mitochondrial membrane markers as indicated. MOM proteins: MAVS, Mfn1, Mfn2 and Tom20. IMS protein: HtrA2. MIM proteins: AIF, OPA-1 and CoxIV. Matrix proteins: Tfam and mtHsp70. (e) HEK293 cells were co-transfected with 5 ng of NLuc-PB1-F2 (88W) expression plasmid with increasing amounts (0–200 ng) of either Venus(N)-PB1-F2 (88W) (open triangle), Venus(C)-PB1-F2 (88W) (open circle), or equal mass pairs of Venus(N)- and Venus(C)-PB1-F2 (88W) (filled square) expression plasmids and were analyzed 21 h later using a biomolecular fluorescence complementation BRET saturation assay. Inset figure depicts the dose-dependent complementation (Venus(N + C)-PB1-F2 (88W)) of Venus fluorescence signal. All data represent the mean values ± s.d. (n = 3 experiments).

Tom40-dependent import of PB1-F2 into mitochondria. Having identified that PB1-F2 is imported into the mitochondrial IMS, we next investigated whether this protein could be transported via the translocase of the outer membrane (TOM) machinery of the host import system²⁷. Using an RNA interference approach, we treated HeLa cells with representative TOM-specific (*TOM22*-, *TOM40*-, or *TOM70*-) small interference RNAs (siRNAs) and confirmed that the target Tom proteins were efficiently suppressed by >80% (Fig. 3a).

As expected, the knockdown of Tom40, which is a major MOM import channel, clearly inhibited the import of mitochondrial matrix-targeted enhanced green fluorescent protein (Su9-eGFP; Fig. 3b; middle images); however, the integration of MOM proteins (Omp-25, MARCH-V/MITOL and Mfn2) was unaffected by Tom40 depletion (Supplementary Fig. 6a–c) as reported previously²⁸. We observed that the mitochondrial import of

PB1-F2 was also greatly suppressed by Tom40 knockdown, resulting in a clear diffuse cytosolic distribution (Fig. 3c, middle images). To eliminate the possibility of off-target effects, we tested secondary siRNAs against *TOM40*, and both pairs of oligos (*TOM40_#B* and *TOM40_#C*) caused similar impairment of PB1-F2 incorporation into mitochondria as observed with the Su9-eGFP construct (Supplementary Fig. 7a). By contrast, knockdown of Tom70, which is an essential component of the translocation of MOM proteins with a multi-spanning transmembrane domain²⁸, did not affect mitochondrial import of either Su9-eGFP or PB1-F2 (Fig. 3b,c, bottom images and Supplementary Fig. 7a), although the integration of the polytopic MOM proteins MARCH-V/MITOL and Mfn2, which were used as controls, was significantly inhibited by Tom70 depletion (Supplementary Fig. 6b,c).

Intriguingly, we demonstrated that PB1-F2 translocation into mitochondria did not rely on the canonical TOM machinery

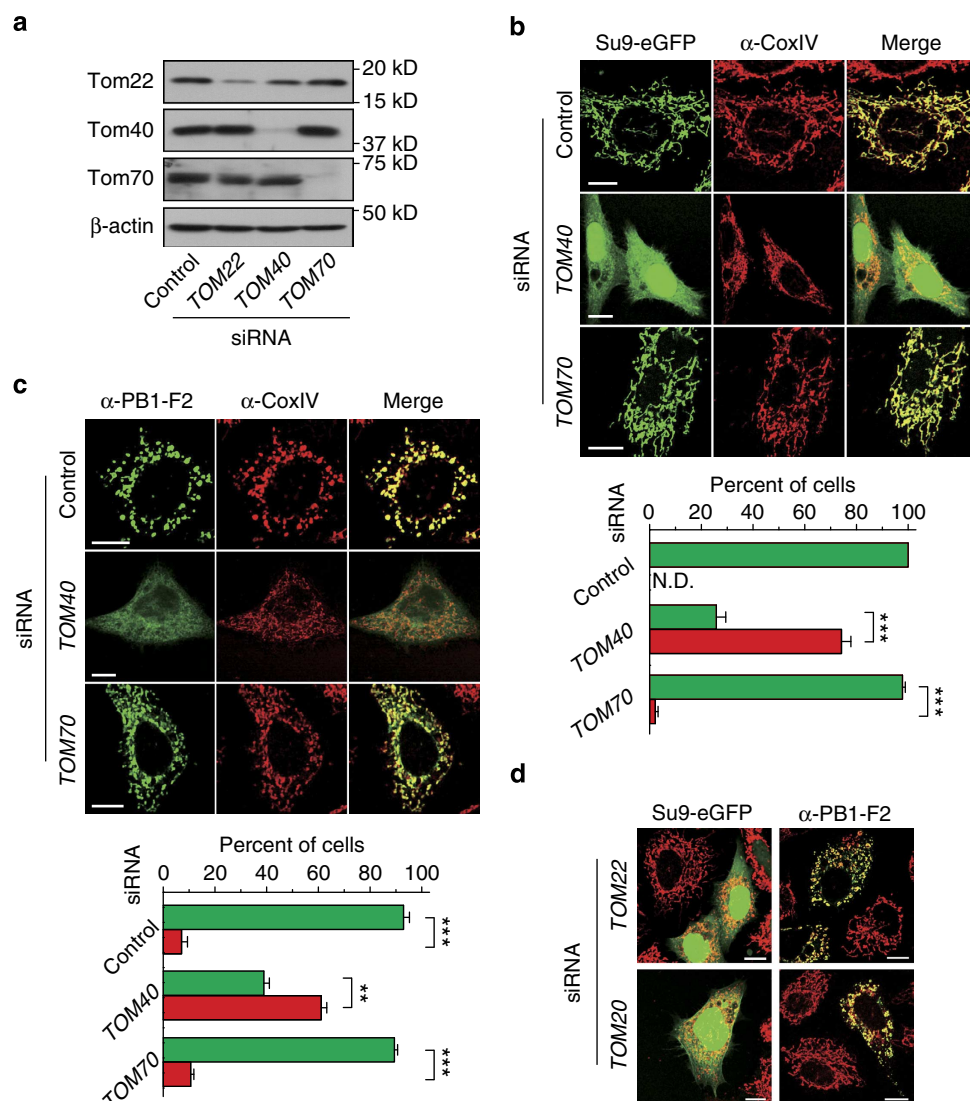


Figure 3 | PB1-F2 translocation into mitochondria depends on Tom40 channels. (a) HeLa cells were treated with either control siRNA or siRNA directed against representative TOM components (*TOM22*, *TOM40* and *TOM70*) to evaluate the effect of PB1-F2 import into mitochondria. The silencing efficiency for each Tom protein was confirmed by immunoblotting with specific antibodies, and β-actin was used as a loading control. (b,c) Subcellular localization of (b) mitochondrially targeted enhanced GFP (Su9-eGFP) and (c) PB1-F2 (PR8) in the siRNA-treated HeLa cells (*TOM40* and *TOM70*). In each *in vivo* import experiment, at least 150 cells were scored, and the green and red bars represent mitochondrial and cytosolic localization, respectively. All data represent the mean values ± s.d. ($n=3$ experiments). Scale bar, 10 μm. N.D., not detected, ** $P<0.01$ and *** $P<0.001$ (by unpaired *t*-test). (d) Immunofluorescence images of the subcellular localization of Su9-eGFP or PB1-F2 (PR8) in HeLa cells treated with either *TOM22* or *TOM20* siRNAs. Scale bar, 10 μm.

because the attenuation of endogenous Tom20 or Tom22 production, which are central import receptors that recognize the positively charged N-terminal presequence of proproteins, did not affect PB1-F2 localization in mitochondria (Fig. 3d and Supplementary Fig. 7b). Indeed, *in silico* analysis revealed the absence of the mitochondrial targeting sequence (MTS) in PB1-F2 proteins (Supplementary Fig. 8a), and substitutions of basic residues predicted to be essential for mitochondrial targeting²¹ did not alter its translocation (Supplementary Fig. 8b). Specifically, the omission of several basic residues from the C-terminal region of PB1-F2 potentially destabilized the mutant proteins *in vivo* (Supplementary Fig. 8c). Taken together, these findings indicate that the translocation mechanism of the viral protein into mitochondria is distinct from the canonical host-protein import system that is generally mediated by Tom20/Tom22 receptors (and Tom70 for precursors with a hydrophobic presequence), which might account for the unique structural properties of the MTS in PB1-F2.

Defective mitochondrial dynamics in PB1-F2-expressing cells.

In the course of examining PB1-F2 import into mitochondria, we found that the morphological balance of mitochondrial networks was extensively shifted towards fragmented structures in the A/PR8-infected cells compared with uninfected cells (Fig. 4a and Supplementary Fig. 9). When the cells were challenged against the A/CA/04/09 strain, which naturally lacks the PB1-F2 gene (Supplementary Fig. 1a; encoding only 11 amino acids), the vast majority of mitochondria exhibited morphologies similar to uninfected cells (Fig. 4a, bottom panels and Supplementary Fig. 9). We therefore quantified mitochondrial morphology in PB1-F2-expressing cells, and confirmed that >50% of the population exhibit fragmented mitochondria (Fig. 4b; red bar). This phenomenon was also observed in cells that transiently expressed full-length PB1-F2 variants, whereas Mock- and 12S variant-transfected cells exhibited no obvious abnormal phenotypes (Fig. 4c). Interestingly, the accumulation of punctate mitochondria in PB1-F2-expressing cells was unrelated to the expression level of mitochondrial GTPases (Drp-1, Mfn1 and Mfn2) involved in mitochondrial dynamics, with the exception of a slight reduction in long OPA-1 isoforms (L-OPA-1), which regulate mitochondrial fusion (Fig. 4d). These findings suggest that the accumulation of PB1-F2 in mitochondria causes defects in mitochondrial dynamics and raises the possibility that the physiological function of PB1-F2 is to modulate mitochondrial-mediated cellular functions.

Mitochondrially translocated PB1-F2 attenuates $\Delta\psi_m$. We investigated $\Delta\psi_m$ in PB1-F2-expressing cells because reduction of L-OPA-1 by proteolytic processing is a $\Delta\psi_m$ -dependent process²⁹. Although mitochondria in uninfected cells were uniformly stained with the $\Delta\psi_m$ -sensitive dye MitoTracker Red (Fig. 4e; top image), mitochondria in the A/PR8-infected cells displayed non-uniform staining, and these less intensely stained mitochondria likely correlated with PB1-F2 co-localization (bottom figures, circled areas). In line with these observations, HeLa cells transfected with full-length PB1-F2 variant plasmids exhibited similar patterns of widespread loss of $\Delta\psi_m$, but these dimly stained mitochondria were not observed in cells expressing the 12S variant or in A/CA/04/09-infected cells (Supplementary Fig. 10).

Moreover fluorescence-activated cell sorting (FACS) analysis verified the relationship between $\Delta\psi_m$ and PB1-F2 expression because the fluorescence intensity of another $\Delta\psi_m$ -sensitive dye, tetramethylrhodamine methyl ester (TMRM), was significantly decreased in A/PR8-infected cells (Fig. 5a; red line in the right

panel) compared with uninfected cells (black line). We hypothesized that this effect was due to the accumulation of PB1-F2 in mitochondria because cells transfected with plasmids encoding full-length PB1-F2 variants also retained the $\Delta\psi_m$ -decreased phenotype (Fig. 5b; PR8 and 88W), although other influenza A viral M2 proteins, a proton-selective ion channel, and 12S failed to demonstrate this effect (Fig. 5b and Supplementary Fig. 11a).

We then monitored the kinetic profile of PB1-F2 expression and its $\Delta\psi_m$ reduction in J774A.1 macrophages infected with A/PR8. The $\Delta\psi_m$ of the infected cells as detected by Mitoprobe JC-1 started to decrease at ~9 h post infection (Fig. 5c; left panel), and this profile matched the expression pattern of PB1-F2 (right blots) as well as L-OPA-1 processing within the cells (Fig. 5c, bands a and b; and Supplementary Fig. 11b). The translocation of PB1-F2 into mitochondria was not affected by CCCP-treatment (Fig. 5d) perhaps because the protein could not cross the MIM (Fig. 2). Taken together, these observations indicate that mitochondrially targeted PB1-F2 leads to the attenuation of $\Delta\psi_m$.

PB1-F2 functions upstream in mitochondrial fission pathway.

Given that the accumulation of PB1-F2 in mitochondria leads to remarkable mitochondrial fragmentation, we attempted to elucidate whether certain molecules involved in mitochondrial dynamics correlate with this phenomenon. PB1-F2-induced mitochondrial fragmentation was not observed in cells treated with Drp-1-specific siRNA, rather extensively elongated tubules were noted (Fig. 6a; middle row; PR8, 88W and 58W). These phenotypes indicate that the mitochondrial fission observed in wild-type cells occurs via a Drp-1-dependent pathway, and PB1-F2 acts upstream of Drp-1 in the cascade. We next tested the effect of PB1-F2 in cells with attenuated endogenous OMA-1, a mitochondrial zinc metallopeptidase, because the protease mediates L-OPA-1 degradation and negatively regulates mitochondrial fusion under stress conditions³⁰. In these cells, mitochondria remain to be elongated structures, even in the presence of PB1-F2 variants, with no obvious punctate mitochondria (Fig. 6a,b). These results demonstrate that the viral protein acts upstream of OMA-1. Collectively, these findings highlight the mechanism for PB1-F2 involvement in the early pathway of mitochondrial fission (Fig. 6c) and potentially link this process to OMA-1 activation.

PB1-F2 inhibits the RIG-I signalling pathway. The aforementioned experiments indicated that the influenza A viral protein PB1-F2 has the potential to interfere with fundamental mitochondrial function. To evaluate the physiological relevance of this protein in host cells, we sought to determine the effect of PB1-F2 on a mitochondrial-mediated immune response, the RIG-I signalling pathway. We examined whether the mitochondrial translocation of PB1-F2 modulates the RIG-I-mediated activation of IFN- β and nuclear factor κ B (NF- κ B) reporter constructs. The overexpression of Myc-tagged MAVS, the downstream adaptor molecule of RIG-I, potently activated both IFN- β and NF- κ B luciferase reporters (Fig. 7a,b; black bars) as described previously³¹. However, the co-expression of full-length PB1-F2 variants, but not 12S, with MAVS was sufficient to inhibit the MAVS-dependent activation of the RIG-I signalling pathway in a dose-dependent manner (Fig. 7a,b; PR8, 88W and 58W), even with equal amounts of MAVS expression (inset blots) or its mitochondrial localization (Supplementary Fig. 12). The inhibitory activities of PB1-F2 variants were also confirmed by stimulating cells transfected with a plasmid that expresses RIG-I, which is the upstream molecule of MAVS (Supplementary Fig. 13a). In addition, the delivery of poly(I:C) into HEK293

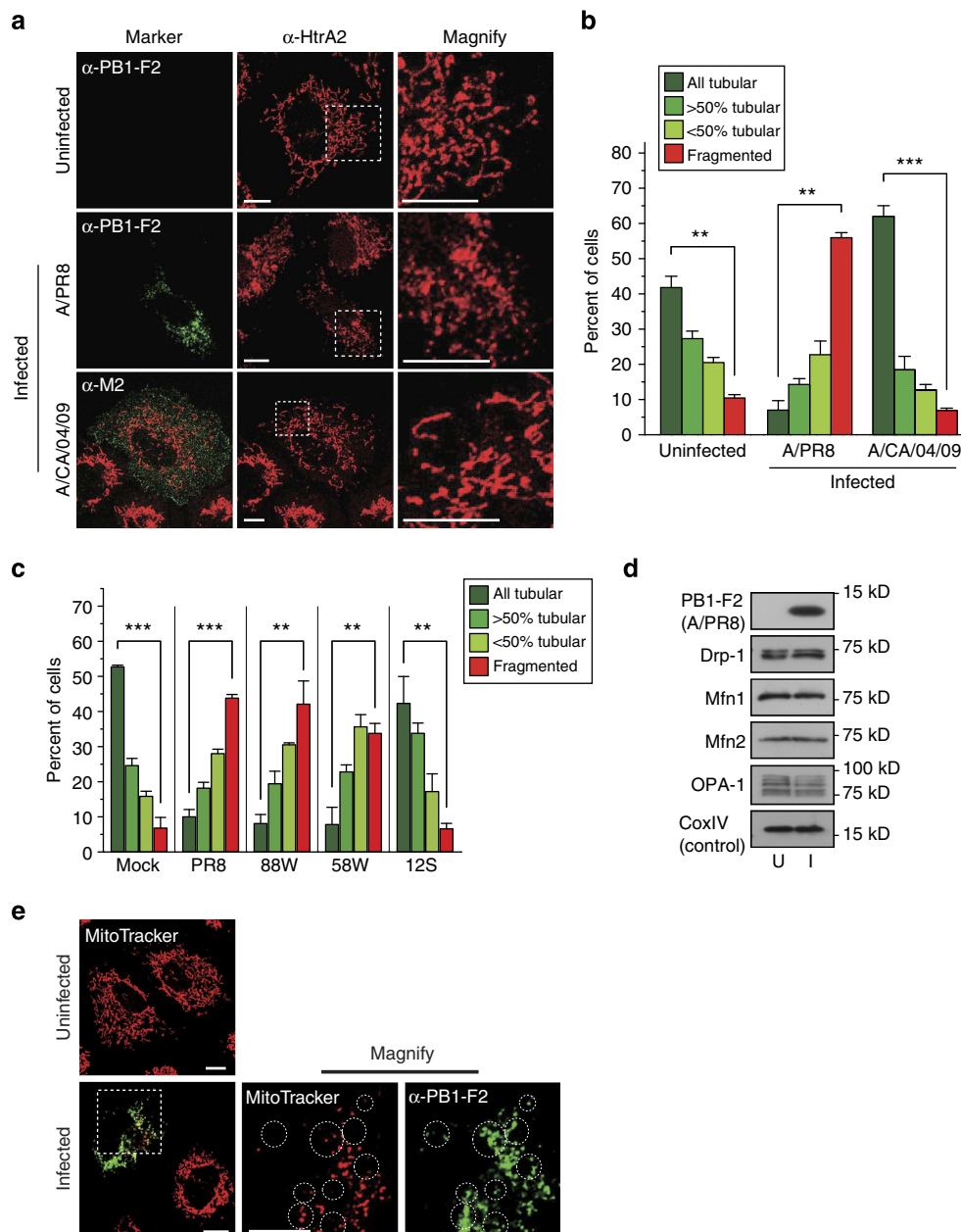


Figure 4 | Defects in mitochondrial tubular networks induced by PB1-F2 expression. (a) A549 cells were infected with either the A/PR8 (16 HA U ml⁻¹) or A/CA/04/09 (multiplicity of infection (MOI) of 10) strains for 22 h, and the mitochondrial morphology of infected cells was monitored by immunofluorescence microscopy (left panels). Mitochondria in the same cells were stained with an anti-HtrA2 polyclonal antibody (middle panels). Images on the right depict a magnified version of the boxed areas in each middle image. To detect A/CA/04/09-infection, an anti-M2 monoclonal antibody was used. (b) Quantification of mitochondrial morphology in a. Cells were scored as one of the four morphological categories as depicted in the inset. In each infection experiment, at least 100 cells were scored. (c) HeLa cells were transfected with each PB1-F2 variant plasmid, and their mitochondrial morphologies were classified. In each transfection experiment, at least 100 cells were scored. (d) Protein expression levels (Drp-1, Mfn1, Mfn2 and OPA-1) in the A/PR8-infected (I) and uninfected (U) cells were analyzed by immunoblotting. CoxIV was used as a loading control. (e) A549 cells were infected with A/PR8 (16 HA U ml⁻¹) or uninfected, and the cells were stained with MitoTracker Red CMXRos, which detects mitochondrial membrane potential ($\Delta\psi_m$). The two right panels are magnified images of the boxed area in the infected cells (left panel), and the circles in the images are highlighted examples of mitochondria loss of $\Delta\psi_m$. All data represent the mean values \pm s.d. ($n = 3$ experiments). Scale bar, 10 μ m. ** $P < 0.01$ and *** $P < 0.001$ (by unpaired t -test), respectively.

cells by transient transfection stimulated the phosphorylation of endogenous IFN regulatory factor 3 (IRF-3), a hallmark of IRF-3 activation, which was suppressed by full-length PB1-F2 variants (Supplementary Fig. 13b). Consistent with these findings, the production of the endogenous proinflammatory cytokine IL-6 in response to A/PR8 infection was substantially downregulated

compared with the A/Beijing/262/1995 (H1N1) strain that encodes a 57 amino acid PB1-F2 (Supplementary Fig. 13c). Furthermore, the cells decreased $\Delta\psi_m$ due to the expression of full-length PB1-F2 variants were more susceptible to infection by a recombinant vesicular stomatitis virus than cells expressing 12S due to defective mitochondrial-mediated

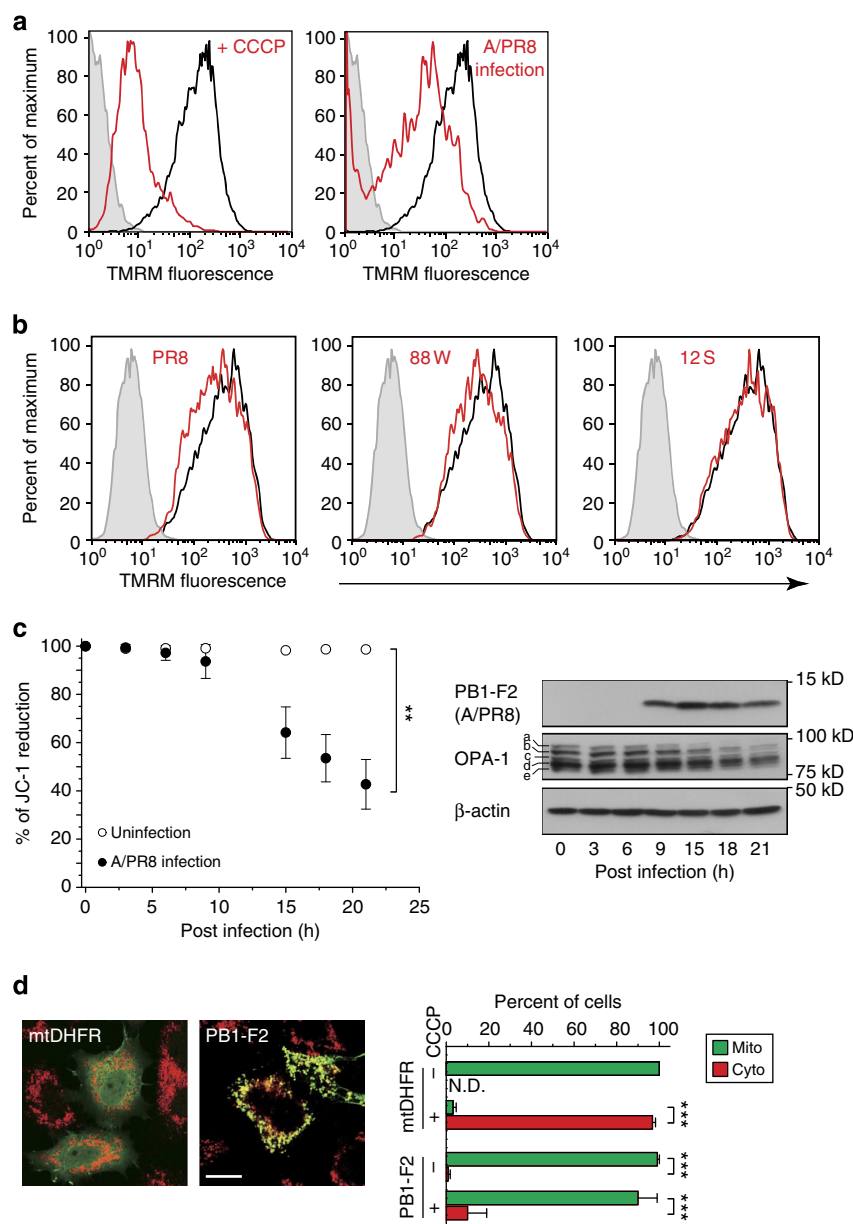


Figure 5 | Mitochondrial-targeted PB1-F2 and its effect on $\Delta\psi_m$. (a) HEK293 cells were infected with A/PR8 (16 HA U ml^{-1}) for about 15 h, and the cells were stained with the cationic fluorescent dye TMRM and analyzed by flow cytometry (right panel; red trace). As a control, CCCP-treated cells ($40 \mu\text{M}$) were also analyzed (left panel). Grey histograms in both panels represent a profile of unstained cells. (b) Similar to a, except that HEK293 cells were transfected with the expression plasmid indicated inside the panel. Cells were analyzed by flow cytometry at 24 h post transfection. (c) The kinetics of $\Delta\psi_m$ disruption in A/PR8-infected J774A.1 macrophages. Cells infected with A/PR8 were collected at the indicated time points (0, 3, 6, 9, 15, 18 and 21 h), stained with JC-1 for 30 min, and analyzed by flow cytometry. The percentage of JC-1 reduction (y axis) is presented. The immunoblot on the right represents a profile of PB1-F2 expression at each time point as well as the loading controls β -actin and OPA-1. Five bands (a–e) of OPA-1 isoforms were detected by immunoblotting with the antibody against OPA-1, and bands a and b are a mixture of L-OPA-1 isoforms. (d) $\Delta\psi_m$ is dispensable for PB1-F2 translocation into mitochondria. HeLa cells transfected with either mitochondrial-targeted dihydrofolate reductase (mtDHFR) or PB1-F2 were treated with (+) or without (–) CCCP ($40 \mu\text{M}$), and their translocation into mitochondria was monitored by immunofluorescence microscopy (left images). Quantification is listed in the right score panel. In each transfection experiment, at least 100 cells were scored, and the green and red bars represent mitochondrial and cytosolic localization, respectively. All data represent the mean values \pm s.d. ($n = 3$ experiments). Scale bar, $10 \mu\text{m}$. N.D., not detected, $**P < 0.01$ and $***P < 0.001$ (by unpaired t -test).

immunity (Supplementary Fig. 13d). Verifying that the observed inhibitory effects of PB1-F2 were not due to the induction of apoptosis under our experimental conditions, we confirmed that cells expressing full-length variants remained viable by examining cytochrome c release (Supplementary Fig. 14a) or activation of caspase-3 or poly (ADP-ribose) polymerase (PARP; Supplementary Fig. 14b).

To test whether the topology of PB1-F2 in mitochondria is essential for its inhibitory effect on signalling events, we designed chimeric proteins expected to incorrectly localize to the MOM. We fused a C-terminal transmembrane segment from Omp-25, which is a MOM protein, with PB1-F2 variants and confirmed that these mutants (PR8-Omp25 and 88W-Omp25) were integrated into the MOM without attenuating $\Delta\psi_m$

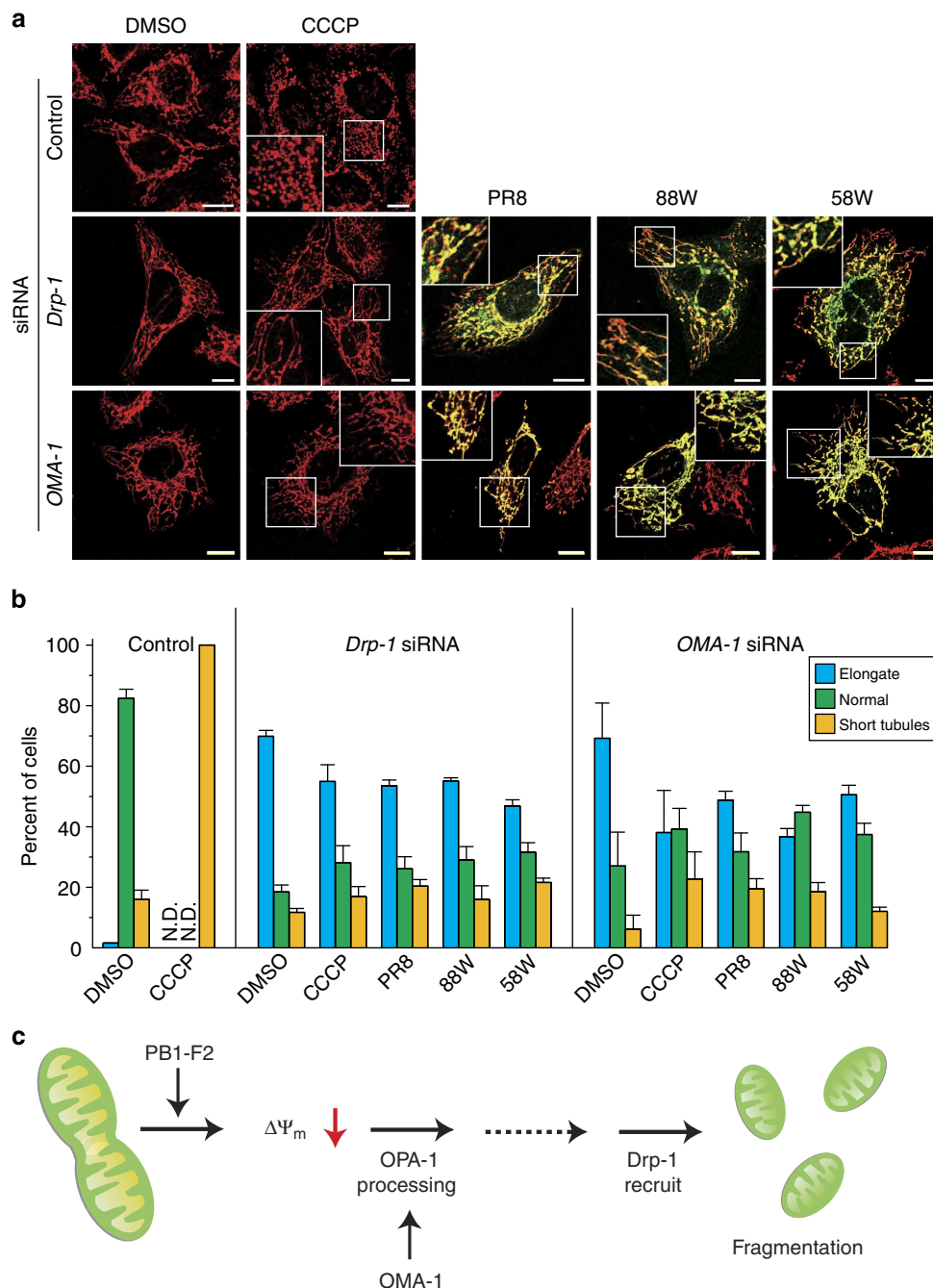


Figure 6 | Knockdown of *Drp-1* or *OMA-1* inhibits PB1-F2-induced mitochondrial fission. (a) Mitochondrial morphology in HeLa cells treated with control siRNA, *Drp-1* siRNA or *OMA-1* siRNA. Each siRNA-treated cell was transfected with PB1-F2 expression plasmids as indicated or treated with 20 μ M CCCP (DMSO as a control). PB1-F2-expressing cells were identified by immunofluorescence, and mitochondria were visualized using an antibody against CoxIV. Insets depict the magnified images of each boxed area. Scale bar, 10 μ m. (b) Quantification of mitochondrial morphology in a. Cells were scored as one of three morphological categories as shown in the inset. In each transfection experiment, at least 100 cells were scored. All data represent the mean values \pm s.d. ($n = 3$ experiments). N.D., not detected. (c) Model of mitochondria fission induced by PB1-F2. We propose that the observed mitochondrial fragmentation occurs via a Drp-1-dependent pathway.

(Supplementary Fig. 15a,b). Strikingly, neither of the chimeric proteins exhibited any functional effect on the RIG-I-mediated activation of IFN- β compared with intact proteins (Fig. 7c). We believe that PB1-F2-induced inhibition of the RIG-I pathway was not attributable to a jamming of MAVS oligomerization, because the presence of PB1-F2 variants did not interfere structurally with the MAVS–MAVS interaction (Supplementary Fig. 16). Together, these findings demonstrate that PB1-F2 acts downstream of

MAVS activation and impairs RLRs-dependent antiviral signaling, further highlighting the importance of $\Delta\Psi_m$ in upregulating MAVS-mediated signal transduction^{16,32}.

PB1-F2 inhibits the activation of NLRP3 inflammasomes. Apart from the RIG-I signalling pathway, mitochondria also act as a platform for activating NLRP3 inflammasomes, which are

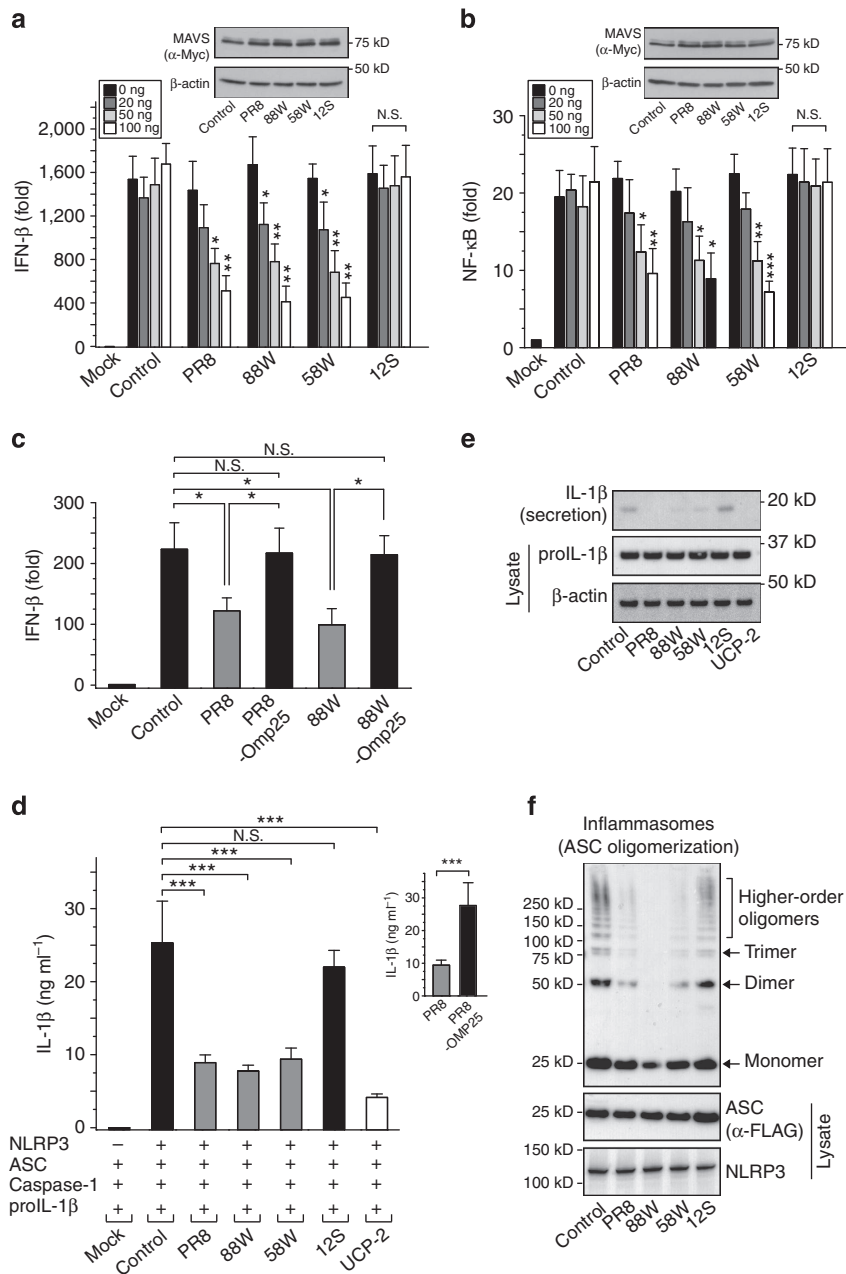


Figure 7 | The effect of mitochondrial-targeted PB1-F2 in antiviral innate immunity. (a,b) HEK293 cells were co-transfected with 75 ng of plasmid encoding Myc-tagged MAVS, increasing amounts (20, 50 and 100 ng) of plasmids encoding the PB1-F2 variants, and either the (a) IFN- β or the (b) NF- κ B reporter plasmids. Transfected cells were analyzed 24 h later for reporter gene-dependent luciferase activities. In these assays, we used Su9-eGFP plasmids as the control. Western blots reveal the abundance of Myc-MAVS proteins. (c) HEK293 cells were co-transfected with 75 ng of plasmid encoding Myc-tagged RIG-I (1-250), 100 ng of PB1-F2 chimeric mutants, and IFN- β reporter plasmids. (d) HEK293 cells were co-transfected with 30 ng of plasmid encoding NLRP3, ASC (5 ng), procaspase-1 (5 ng), pro-IL-1 β (150 ng) and each PB1-F2 variant (300 ng). Cell-free supernatants were collected 24 h post transfection, and secreted IL-1 β was measured by ELISA. In these assays, we used the eGFP plasmid as the control. Inset: the functional role of the MOM-localized PB1-F2 chimeric mutant in NLRP3 inflammasomes. (e) The reconstituted level of secreted IL-1 β in d was confirmed by immunoblotting with antibodies against human IL-1 β and pro-IL-1 β , and β -actin was used as a loading control in whole cell lysates. (f) The inhibition of ASC oligomerization by mitochondrial-targeted PB1-F2 variants. HEK293 cells transfected with plasmids encoding NLRP3, FLAG-tagged ASC, and each PB1-F2 variant were lysed and their lysates were cross-linked with BS3. The samples were analyzed by immunoblotting with antibody against FLAG. The bottom blots confirm the expression levels of NLRP3 and ASC proteins in their lysates. All data represent the mean values \pm s.d. ($n = 3$ experiments). N.S., not significant, $*P < 0.05$, $**P < 0.01$, and $***P < 0.001$ (by unpaired t -test), respectively.

involved in early stages of the inflammatory response by sensing cellular damage or stress, including viral infection^{12–14,17,33}. The activation of NLRP3 inflammasomes is initiated via the formation of a multi-complex with an adaptor protein, apoptosis-associated speck-like protein containing a caspase recruitment domain

(ASC) and procaspase-1. This association is followed by the processing of procaspase-1 to its mature form, which ultimately leads to IL-1 β maturation³⁴. We reconstituted NLRP3 activation by co-transfecting cells with NLRP3, ASC, procaspase-1 and pro-IL-1 β expression plasmids and evaluated the secretion of IL-1 β

in vitro (Fig. 7d; control) as described previously^{35,36}. In addition to the RIG-I pathway, the expression of full-length PB1-F2 variants (PR8, 88W, and 58W) significantly suppressed the secretion of IL-1 β , similar to the uncoupling protein 2 (used as a positive control¹⁷), whereas 12S abolished the effect (Fig. 7d,e) despite similar cytosolic pro-IL-1 β expression level (Fig. 7e; middle blot). Again, MOM-localized PB1-F2 mutants were unaffected by the inactivation of NLRP3 inflammasomes (Fig. 7d inset figure, and Supplementary Fig. 15c). Interestingly, when cells were treated with *TOM40* siRNA, the suppression of IL-1 β induced by the full-length PB1-F2 variants was also less complete, resulting in the recovery of NLRP3 activation (Supplementary Fig. 15d). These findings demonstrate that mitochondrially targeted PB1-F2 acts as a negative regulator of NLRP3 inflammasomes.

We also examined ASC oligomerization, the hallmark assembly of activated NLRP3 inflammasomes, in the presence of PB1-F2 variants. Reduced accumulation of higher-order oligomers was exclusively observed when the mitochondrially targeted version of the variants was present (Fig. 7f). In addition, we confirmed that NLRP3 recruitment to mitochondria, an upstream event of NLRP3 inflammasome formation³³, was prohibited by the presence of PB1-F2 (Supplementary Fig. 17).

Taken together, these data demonstrate that $\Delta\psi_m$ dissipation introduced by translocation of the influenza A virus PB1-F2 into mitochondria correlates with the severity of defective mitochondrial-mediated innate immunity, including the RIG-I signalling pathway and activation of NLRP3 inflammasomes.

Discussion

Some viruses encode genes that have the potential to suppress host cell immunity due to a viral evasion strategy. An example of such a gene product is the hepatitis C virus serine protease NS3/4A, which proteolytically cleaves MAVS and ultimately abolishes mitochondrial-mediated antiviral signalling^{37,38}. The influenza A virus also encodes several gene products that aid in escaping immune responses, for example, nonstructural protein 1, an inhibitor of the RIG-I pathway through its binding to RIG-I³⁹, and PB1-F2, which downregulates mitochondrial-mediated immune responses by attenuating $\Delta\psi_m$ as demonstrated in the present study.

The gene product PB1-F2, which is encoded by a +1 reading frame shift of PB1, is a unique polypeptide with naturally existing variants of various lengths ranging from 11 to 87 or 90 amino acids. It is curious that a highly pathogenic (H5N1) subtype and pandemic (1918, 1957 and 1968) strains of influenza A virus tends to encode longer polypeptides; thus, we presumed that this molecular signature might affect pathogenicity (Supplementary Fig. 1). In this regard, previous studies demonstrated that PB1-F2 with 87 amino acids colocalizes with mitochondria^{18,20–22}, and its targeting is proposed to be caused by the C-terminal region of the polypeptide that acts as an MTS^{20,21} and is frequently missing in the low pathogenic subtypes (Supplementary Fig. 1). Consistent with these assumptions, we demonstrated that full-length versions of PB1-F2 from different viral strains specifically translocate into mitochondria, and we further revealed mechanistic insight into how the viral protein is incorporated into the organelle.

We first demonstrated that PB1-F2 localizes to the mitochondrial IMS and tightly associates with the MIM (Fig. 2). A sequence profile of PB1-F2, which has an extremely basic isoelectric point (\sim pKa > 10), supports the notion that PB1-F2 has an electrostatic interaction with its negatively charged membrane. We next observed that the membrane-associated PB1-F2 forms a stable homotypic complex at the membrane and

that the complex is a highly ordered assembly that contains more than three molecules (Fig. 2e). Given that the accumulation of PB1-F2 in mitochondria causes defects in mitochondrial function as described in the following section, this complex would presumably interact with other mitochondrial proteins. Finally, we clarified that PB1-F2 translocation into the mitochondria relied on a specific TOM component, the Tom40 import channel (Fig. 3). Interestingly, our *in vivo* import analysis clearly demonstrated that PB1-F2 bypasses the general import receptors Tom20/Tom22 and is targeted directly to the Tom40 channel likely by evading host cell surveillance during import. Collectively, our findings provide a mechanism for PB1-F2 import into mitochondria and localization in mitochondrial sub-compartments. Further studies are needed to identify other viral proteins (includes another influenza A viral protein) that have an affinity for mitochondria and to elucidate whether these proteins hijack the host import machinery.

Our results from influenza A-infected cells clearly demonstrate that PB1-F2 translocates into mitochondria, leading to a loss of $\Delta\psi_m$, which results in abnormal fragmented mitochondria (Fig. 4; Supplementary Figs 9 and 10). The most likely explanation for the dissipation of $\Delta\psi_m$ by PB1-F2 is that the formation of positively charged PB1-F2 oligomers on the MIM leads to some functional defects in the respiratory chain complexes and ultimately to widespread heterogeneity of $\Delta\psi_m$. Importantly, PB1-F2-induced mitochondrial fragmentation was not observed in cells in which either Drp-1 or OMA-1 were individually depleted by siRNA treatment, suggesting that mitochondrial fission occurs via a Drp-1-dependent pathway (Fig. 6). In particular, OMA-1-mediated processing of L-OPA-1 is a stress-related cellular response³⁰, and thus it we speculate that mitochondrially targeted PB1-F2 might trigger OMA-1 activation and induce such punctate mitochondria.

We also revealed that cells with abnormal mitochondria exhibited defective mitochondrial-mediated innate immune responses, including activation of the RIG-I signalling pathway and NLRP3 inflammasomes (Fig. 7). These observations are interesting in light of our previous findings that cells completely lacking mitochondrial fusion due to targeted deletion of both *Mfn1* and *Mfn2* also have severely impaired immune responses against RNA viruses¹⁶. Arnoult and colleagues⁴⁰ reported that OPA-1 knockdown negatively regulates virus-induced activation of the transcriptional factor NF- κ B and depletes the fission factor Drp-1, thereby upregulating the RIG-I signalling pathway. Cellular stress, including viral infection, does not always induce mitochondrial fragmentation^{40,41}, and thus our results highlight the physiological impact of influenza A viral evasion of host immunity via $\Delta\psi_m$ regulation in connection with mitochondrial dynamics. Although we believe that $\Delta\psi_m$ manipulation by PB1-F2 is important in relation to innate immunity, we cannot rule out the possibility that mitochondrially targeted PB1-F2 affects innate immunity via another unknown route. In addition, PB1-F2-induced mitochondrial dysfunction also potentially impacts the pathogenicity of secondary bacterial infections. McCullers and colleagues reported that A/PR8-challenged mice exhibit significant weight loss and have greater susceptibility to pneumonia caused by *Streptococcus pneumoniae*, a Gram-positive bacteria that causes secondary infection⁴². It is notable that the pathogenic phenotypes are diminished when using a truncated version of the PB1-F2 polypeptide^{42,43}, which corresponded to the lack of the C-terminal region that is important for mitochondrial translocation. In general, secondary bacterial infections are associated with increased severity and lethality, and future studies aimed at evaluating the role of PB1-F2 in the differential susceptibility to pathogen infection may prove interesting.